Compact generation scheme of path-frequency hyperentangled photons using 2D periodical nonlinear photonic crystal

Yang-He Chen(陈洋河), Bo Ji(季波), Nian-Qin Li(李念芹), Zhen Jiang(姜震), Wei Li(李维), Yu-Dong Li(李昱东), Liang-Sen Feng(冯梁森), Teng-Fei Wu(武腾飞), and Guang-Qiang He(何广强)
Citation: Chin. Phys. B, 2023, 32 (**12**): 120307. DOI: 10.1088/1674-1056/ad0625
Journal homepage: http://cpb.iphy.ac.cn; http://iopscience.iop.org/cpb

What follows is a list of articles you may be interested in

Generation of hyperentangled photon pairs based on lithium niobate waveguide

Yang-He Chen(陈洋河), Zhen Jiang(姜震), and Guang-Qiang He(何广强)
Chin. Phys. B, 2023, 32 (**9**): 090306. DOI: 10.1088/1674-1056/acd5c4

Faithful and efficient hyperentanglement purification for spatial-polarization-time-bin photon system

Fang-Fang Du(杜芳芳), Gang Fan(樊钢), Yi-Ming Wu(吴一鸣), and Bao-Cang Ren(任宝藏)
Chin. Phys. B, 2023, 32 (**6**): 060304. DOI: 10.1088/1674-1056/aca395

Complete hyperentangled Greenberger-Horne-Zeilinger state analysis for polarization and time-bin hyperentanglement

Zhi Zeng(曾志)
Chin. Phys. B, 2023, 32 (**6**): 060301. DOI: 10.1088/1674-1056/ac9044

Measurement-device-independent one-step quantum secure direct communication

Jia-Wei Ying(应佳伟), Lan Zhou(周澜), Wei Zhong(钟伟), and Yu-Bo Sheng(盛宇波)
Chin. Phys. B, 2022, 31 (**12**): 120303. DOI: 10.1088/1674-1056/ac8f37

Deterministic nondestructive state analysis for polarization-spatial-time-bin hyperentanglement with cross-Kerr nonlinearity

Hui-Rong Zhang(张辉荣), Peng Wang(王鹏), Chang-Qi Yu(于长琦), and Bao-Cang Ren(任宝藏)
Chin. Phys. B, 2021, 30 (**3**): 030304. DOI: 10.1088/1674-1056/abd7d5

Compact generation scheme of path–frequency hyperentangled photons using 2D periodical nonlinear photonic crystal

Yang-He Chen(陈洋河)[1,2], Bo Ji(季波)[1,2], Nian-Qin Li(李念芹)[1,2], Zhen Jiang(姜震)[1,2], Wei Li(李维)[3], Yu-Dong Li(李昱东)[3], Liang-Sen Feng(冯梁森)[3], Teng-Fei Wu(武腾飞)[3], and Guang-Qiang He(何广强)[1,2,†]

[1] *SJTU Pinghu Institute of Intelligent Optoelectronics, Department of Electronic Engineering, Shanghai Jiao Tong University, Shanghai* 200240, *China*
[2] *State Key Laboratory of Advanced Optical Communication Systems and Networks, Department of Electronic Engineering, Shanghai Jiao Tong University, Shanghai* 200240, *China*
[3] *Science and Technology on Metrology and Calibration Laboratory, Changcheng Institute of Metrology & Measurement, Aviation Industry Corporation of China, Beijing* 100095, *China*

(Received 2 August 2023; revised manuscript received 18 October 2023; accepted manuscript online 24 October 2023)

Hyperentanglement is a promising resource for achieving high capacity quantum communication. Here, we propose a compact scheme for the generation of path–frequency hyperentangled photon pairs via spontaneous parametric down-conversion (SPDC) processes, where six different paths and two different frequencies are covered. A two-dimensional periodical $\chi^{(2)}$ nonlinear photonic crystal (NPC) is designed to satisfy type-I quasi-phase-matching conditions in the plane perpendicular to the incident pump beam, and a perfect phase match is achieved along the pump beam's direction to ensure high conversion efficiency, with theoretically estimated photon flux up to 2.068×10^5 pairs·s^{-1}·mm^{-2}. We theoretically calculate the joint-spectral amplitude (JSA) of the generated photon pair and perform Schmidt decomposition on it, where the resulting entropy S of entanglement and effective Schmidt rank K reach 3.2789 and 6.4675, respectively. Our hyperentangled photon source scheme could provide new avenues for high-dimensional quantum communication and high-speed quantum information processing.

Keywords: hyperentanglement, nonlinear photonic crystal, quasi-phase-matching

PACS: 03.67.Bg, 42.65.Lm **DOI:** 10.1088/1674-1056/ad0625

1. Introduction

Quantum entanglement is a fascinating and captivating phenomenon in quantum mechanics. It plays a crucial role in areas such as quantum computing,[1–3] quantum communication,[4–7] quantum cryptography,[8,9] quantum imaging,[10,11] and quantum precision measurement.[12] By harnessing quantum entanglement, we can achieve faster and more secure communication,[13,14] efficient computational methods,[15] and breakthroughs in encryption technology.[16]

Hyperentanglement is an intriguing extension of the phenomenon of quantum entanglement that pushes the boundaries of our understanding and exploration of the quantum world. Hyperentanglement refers to a quantum state with entanglement in multiple degrees of freedom, such as polarization, frequency, path, time, and orbital angular momentum.[17] This intricate entanglement creates a vast and intricate quantum state space, offering unprecedented opportunities for information processing and communication.[18] One of the most fascinating aspects of hyperentanglement is its potential for enhancing quantum communication protocols. By exploiting multiple degrees of freedom, hyperentanglement allows for more efficient transmission of information and increases resistance to noise.[19] Such advancements pave the way for significant applications in secure quantum key distribution,[20,21] quantum teleportation,[22] and quantum cryptography.[23,24]

The generation of hyperentangled photon pairs through the spontaneous parametric down-conversion (SPDC) process in nonlinear photonic crystals (NPC)[25–28] with second-order susceptibility $\chi^{(2)}$ is widely employed in research. Specifically, photonic crystals such as periodically poled lithium niobate (PPLN) and periodically poled potassium titanyl phosphate (PPKTP), designed using quasi-phase matching (QPM) technology, enable a range of optical parametric processes, possessing both high efficiency and flexibility.[29–31] This versatility facilitates advanced scientific investigations into novel quantum entanglement sources, contributing to cutting-edge research in the field.

The state of art technique for fabricating two-dimensional NPCs involves a combination of advanced lithography techniques, materials engineering, and nanofabrication methods. Electron beam (EB) lithography is a high-resolution patterning technique that uses a focused beam of electrons to selectively expose a material.[32] Without any static bias, He *et al.* realized the fabrication of two-dimensional ferroelectric domain-reversed structures in lithium niobate using EB lithography at room temperature.[33] In addition, ultrafast laser writing is also a promising fabrication technique for controlling precise two-dimensional NPC structures, and it can achieve three-dimensional NPC fabrication with nanoscale resolution by either writing or erasing domain structures in the crystal.[34,35]

†Corresponding author. E-mail: gqhe@sjtu.edu.cn

Another commonly used technique in NPC fabrication is electrical poling, which involves applying a high voltage to a specific region of the crystal, resulting in the flipping of its $\chi^{(2)}$. In our work, considering that the two-dimensional NPC we designed only has a resolution at the micrometer scale, it can be easily achieved through electrical poling.

In this paper, we first introduce our compact path–frequency hyperentanglement scheme and basic parameters of the designed nonlinear photonic crystal. Then we give the theoretical model of our hyperentangled source using quantum optics theory. Finally the joint-spectral amplitude (JSA) of the generated photon pair is calculated, with Schmidt decomposition on it, demonstrating a strong frequency correlation between the generated two photons.

2. Overall hyperentanglement scheme

We plan and design specific spontaneous parametric down-conversion processes to generate path–frequency hyperentangled photon pair. SPDC processes will take place when both energy conservation and momentum conservation are satisfied. We design a two-dimensional periodical $\chi^{(2)}$ nonlinear photonic crystal to compensate for the phase mismatch in the SPDC processes, i.e., to satisfy quasi-phase-match conditions in the plane perpendicular to the pump beam. Our theoretical scheme is shown in Fig. 1(a). A type-I ($e \to o+o$) phase-matched 5% MgO-doped lithium niobate is selected as the material of our NPC and the temperature is set as room temperature (25 °C).

Our scheme of path–frequency hyperentanglement totally includes 6 different paths and 2 different frequencies. As shown in Fig. 1(b), each path is labeled by a unique angle θ_i $(i = 1,2,3,4,5,6)$ on the xOy plane, and two generated frequencies ω_1 and ω_2 satisfy the energy conservation $\omega_P = \omega_1 + \omega_2$.

Along the z-axis, the momentum is fully conserved which means a perfect phase match

$$k_P = k_{P,z} = k_{S,z} + k_{I,z} = k_S \cos\varphi + k_I \cos\varphi, \tag{1}$$

where the subscript z refers to the z component and φ is the angle between the signal (or idler) photon's momentum and z-axis. The angle φ can be deduced after the frequencies of pump, signal, and idler are chosen.

However, because of the difference between the frequencies of signal and idler photons, momentum mismatch appears in the xOy plane as follows:

$$\begin{aligned} \Delta k &= |\Delta \boldsymbol{k}| = |\boldsymbol{k}_S + \boldsymbol{k}_I - \boldsymbol{k}_P| \\ &= ||\boldsymbol{k}_S|\sin\varphi - |\boldsymbol{k}_I|\sin\varphi| = |k_S - k_I|\sin\varphi. \end{aligned} \tag{2}$$

In our scheme, we set the wavelength of the pump beam as $\lambda_P = 775$ nm (in vacuum, same below), and choose $\lambda_S = 1530$ nm, $\lambda_I = 1570.5$ nm, which belong to the communication band. Then we can calculate $f_1 = c/\lambda_I = 190.9$ THz and $f_2 = c/\lambda_S = 195.9$ THz. The corresponding refractive indices of pump light, signal light, and idler light are $n_P = 2.1707$, $n_S = 2.2095$, and $n_I = 2.2082$, respectively. According to Eqs. (1) and (2), we can obtain $\varphi = 0.186$ rad and $\Delta k = 0.0443\ \mu\text{m}^{-1}$.

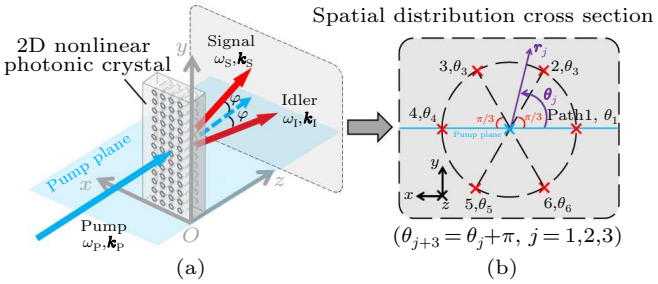

Fig. 1. (a) Our scheme of path–frequency hyperentanglement using a designed two-dimensional NPC. The second order susceptibility $\chi^{(2)}$ of NPC is periodically modified in the xOy plane in order to compensate the momentum mismatch perpendicular to the pump beam. Perfect phase match is achieved along the z axis. (b) Spatial distribution cross section.

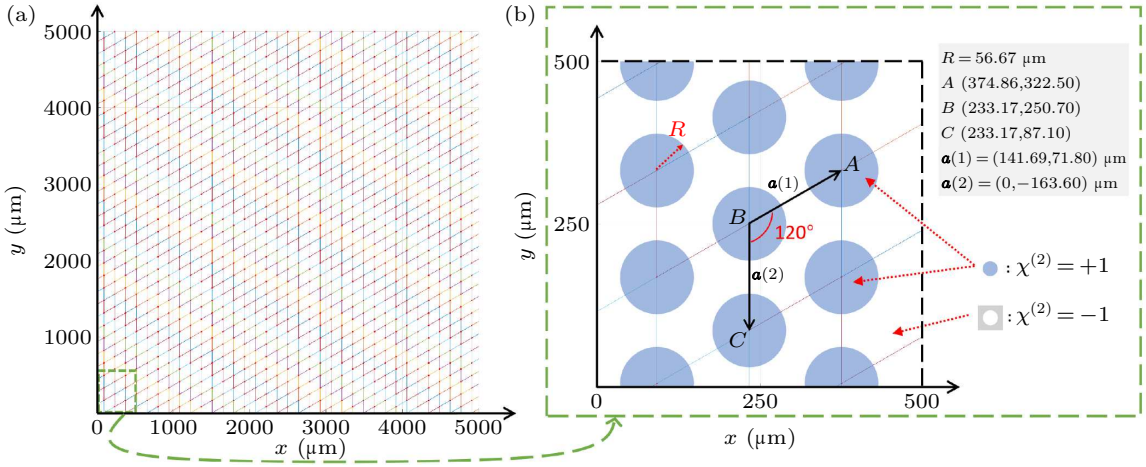

Fig. 2. (a) Lattice structure of the $\chi^{(2)}$ susceptibility design example of our NPC (i.e., $u(\boldsymbol{r})$). (b) Convolution of lattice and circular motif (i.e., $u(\boldsymbol{r}) \otimes s(\boldsymbol{r})$), indicating the distribution of $\chi^{(2)}$ in the xOy plane with accurate structure parameters.

The momentum mismatches of the six SPDC processes have the same numerical value and each possesses a unique direction. That is, the momentum mismatch vectors are evenly distributed on one circumference

$$\theta_i = \frac{(i-1)\pi}{3}, \quad i \in \{1,2,3,4,5,6\}, \tag{3}$$

where θ is the directed angles between the projection of the signal's (or idler's) momentum on the xOy plane and the positive direction of the x-axis, and the subscript i refers to the ith angle of the corresponding SPDC process.

The momentum mismatches can be perfectly compensated through the periodic poling method.[36,37] By periodically modifying the susceptibility of NPC in real space, we can obtain six peak values in its Fourier space (reciprocal space) to perform QPM. The designed distribution of NPC's $\chi^{(2)}$ is shown in Fig. 2.

The second order susceptibility $\chi^{(2)}$ of our NPC can be mathematically expressed as $g(\boldsymbol{r}) = a(\boldsymbol{r}) \times (u(\boldsymbol{r}) \otimes s(\boldsymbol{r}))$, where $a(\boldsymbol{r})$ denotes the area of the NPC, $u(\boldsymbol{r})$ is a sum of delta functions referring to the lattice structure of NPC, and $s(\boldsymbol{r})$ is the motif function.

Circular motif with a radius of 56.67 μm^{-1} is selected. In the motif $\chi^{(2)} = +1$, while $\chi^{(2)} = -1$ in the rest area of the NPC. We fix the relative radius of motif $R/a = 0.2$.

We then further check our design by viewing the NPC in the Fourier domain, as shown in Fig. 3. The six arrows indicate the six mismatch vectors of six SPDC processes. We conclude that the QPM conditions are satisfied using the design.

Using the design example above, we are going to make a brief discussion on the relationship between the direction and frequency of the generated photons. We first fix the azimuth angle of the emitted signal (idler) photons: $\theta_S = 0$, $\theta_I = \pi$, and use the QPM conditions to calculate the relationship between φ_m $(m = S, I)$ and signal photon's wavelength. The results are shown in Fig. 4.

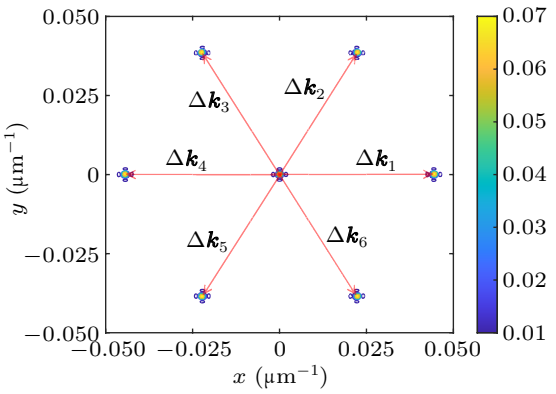

Fig. 3. The $\chi^{(2)}$ susceptibility distribution of designed NPC in Fourier space. The six peaks correspond to six momentum mismatches of expected SPDC processes, which means the QPM conditions are satisfied through the designed NPC.

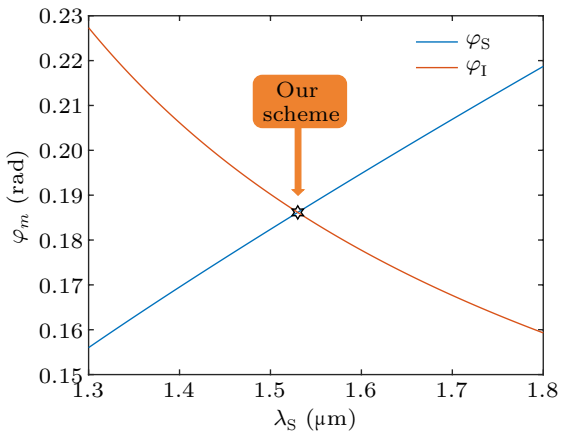

Fig. 4. Relationship between φ_m $(m = S, I)$ and signal photon's wavelength. φ_m $(m = S, I)$ refers to the angle between the pump beam and signal (idler). In our scheme, $\varphi_S = \varphi_I$ ensures the symmetry of signal and idler.

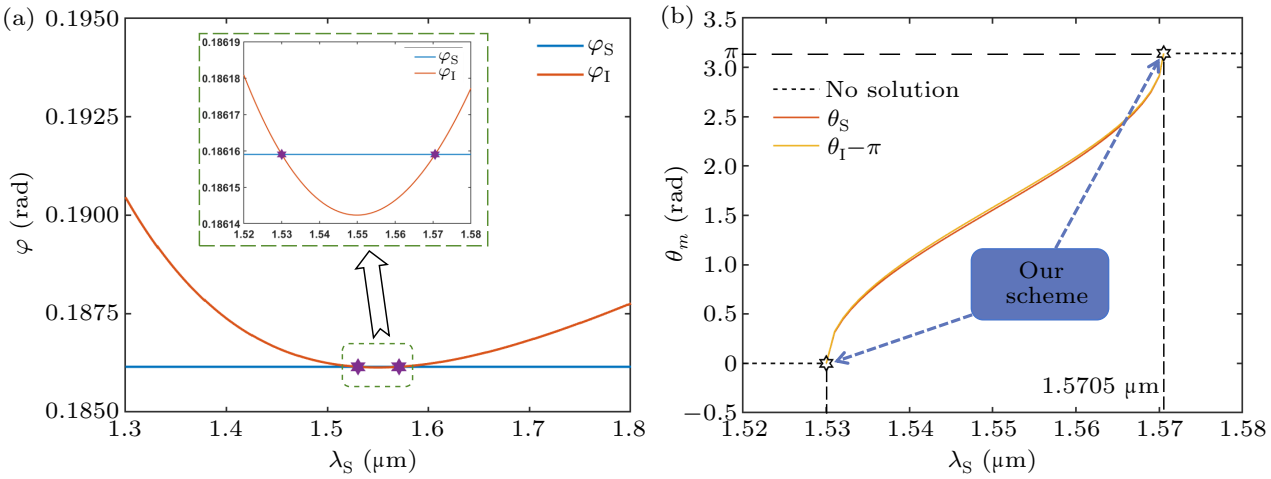

Fig. 5. (a) The angle between pump beam and idler (φ_I) varies with the signal's wavelength (λ_S) when φ_S is fixed, where the perfect phase matching condition is always maintained. The intersection of two curves corresponds to our scheme. Due to the symmetry of f_1 and f_2 with respect to $f_P/2$, there are two intersections in the graph. (b) The azimuth angles of generated photons (θ_m, $m = S, I$) vary with the signal's wavelength (λ_S) when φ is fixed. Two curves are approximately coincident because the signal and idler's wave vectors are much larger than the momentum mismatch compensated by the designed NPC. Both ends of the curve correspond to two of the six expected SPDC processes in our scheme.

Then we fix the angle $\varphi_S = 0.186$ rad to analyze the relationship between other direction angles and signal photon's wavelength. The other three angles are obtained using the three-dimensional vector equation of phase match. The results are shown in Fig. 5.

The analysis above indicates the path–frequency relationship along two orthogonal directions. In fact, our scheme has good scalability and can be easily extended to the case of signal light and idler light at different frequencies, while the calculation and design processes are similar. The angle φ and value of mismatch vector Δk will be different. Therefore, it is necessary to change the poling period of nonlinear photonic crystals. At this point, the NPC's lattice structure $u(\boldsymbol{r})$ needs to be correspondingly reduced or amplified. If we want to expand the number of paths to more than six, we need to utilize quasi-periodic poling nonlinear photonic crystals to compensate for more wave vector mismatches and meet more quasi-phase-matching conditions. However, at this point, due to its Fourier transform domain having smaller peaks at the corresponding mismatch than in the case of periodic poling, and having peaks at other mismatches, the conversion efficiency will decrease.

3. Theoretical model

We will derive the theoretical expression of the generated path–frequency hyperentangled biphoton state. In the interaction picture, the evolution of the quantum state with time satisfies the following equation:[38]

$$|\psi(t\to+\infty)\rangle \approx |\psi(t\to-\infty)\rangle - \frac{\mathrm{i}}{\hbar}\int_{-\infty}^{+\infty}\hat{\boldsymbol{H}}_{\mathrm{int}}(t)|\psi(t\to-\infty)\rangle\,\mathrm{d}t, \quad (4)$$

where $|\psi(t\to-\infty)\rangle = |0\rangle_S|0\rangle_I$, and $\hat{\boldsymbol{H}}_{\mathrm{int}}(t)$ represents the nonlinear part of the three-wave mixing Hamiltonian quantity

$$\hat{\boldsymbol{H}}_{\mathrm{int}}(t) = \epsilon_0\int \mathrm{d}^3\boldsymbol{r}\sum_{\alpha,\beta,\gamma}\chi^{(2)}_{\alpha,\beta,\gamma}(\boldsymbol{r})\boldsymbol{E}^{+}_{\mathrm{P},\gamma}(\boldsymbol{r},t) \times\hat{\boldsymbol{E}}^{-}_{\mathrm{S},\alpha}(\boldsymbol{r},t)\hat{\boldsymbol{E}}^{-}_{\mathrm{I},\beta}(\boldsymbol{r},t)+\mathrm{h.c.}, \quad (5)$$

where h.c. denotes the Hermitian conjugate. Substituting Eq. (5) into Eq. (4) and disregarding the contribution of vacuum, we can derive the two-photon state $|\psi\rangle$ as follows:

$$|\psi\rangle \propto \int_{-\infty}^{+\infty}\mathrm{d}t\int \mathrm{d}^3\boldsymbol{r}\sum_{\alpha,\beta,\gamma}\chi^{(2)}_{\alpha,\beta,\gamma}(\boldsymbol{r})\boldsymbol{E}^{+}_{\mathrm{P},\gamma}(\boldsymbol{r},t) \times\hat{\boldsymbol{E}}^{-}_{\mathrm{S},\alpha}(\boldsymbol{r},t)\hat{\boldsymbol{E}}^{-}_{\mathrm{I},\beta}(\boldsymbol{r},t)|0\rangle_S|0\rangle_I. \quad (6)$$

We consider the input pump light as a classical electric field

$$\boldsymbol{E}^{+}_{\mathrm{P},\gamma}(\boldsymbol{r},t) = \int \mathrm{d}\omega_P A_P(\omega_P)\boldsymbol{E}_P(\boldsymbol{r},\omega_P)\,\mathrm{e}^{-\mathrm{i}\omega_P t},$$

$$\boldsymbol{E}_P(\boldsymbol{r},\omega_P) = \boldsymbol{e}_P(\boldsymbol{r},\omega_P)\,\mathrm{e}^{\mathrm{i}k_P(\omega_P)z-\alpha_P(\omega_P)z}, \quad (7)$$

where $A_P(\omega_P)$ denotes the spectral amplitude of the pump light. The field operators of the signal and idler modes are

$$\hat{\boldsymbol{E}}^{-}_{m}(\boldsymbol{r},t) = \int_{Br_1}\mathrm{d}k_m\sqrt{\frac{\hbar\omega_m(k_m)}{2}}\,\mathrm{e}^{\mathrm{i}\omega_m t}\boldsymbol{E}^{*}_{m}(\boldsymbol{r},k_m)\hat{a}^{\dagger}_{m,k_m},$$
$$\boldsymbol{E}_m(\boldsymbol{r},k) = \boldsymbol{e}_m(\boldsymbol{r},k)\frac{\mathrm{e}^{\mathrm{i}\boldsymbol{k}_m\cdot\boldsymbol{r}}}{\sqrt{2\pi}}, \quad (8)$$

where $m = \mathrm{S},\mathrm{I}$ denotes signal (S) and idler (I), respectively. $\boldsymbol{e}_\mathrm{p}$, $\boldsymbol{e}_\mathrm{s}$, and $\boldsymbol{e}_\mathrm{I}$ are electric field profile of the Bloch mode for pump, signal and idler mode, respectively. Λ and L are the poling period and length of our crystal, respectively. Notation $\int_{Br_1}$ represents the integration of Bloch wave on the first Brillouin zone in the xOy plane. Substituting Eqs. (7) and (8) into Eq. (6), we can obtain

$$|\psi\rangle \propto \iint_{Br_1}\mathrm{d}k_S\,\mathrm{d}k_I\sqrt{\omega_S\omega_I}A_p\frac{\mathrm{e}^{\mathrm{i}\Delta k_z L}-1}{\mathrm{i}\Delta k_z}\int\mathrm{d}^2\boldsymbol{r}_\perp\sum\chi^{(2)}(x,y) \times\mathrm{e}^{\mathrm{i}\Delta\boldsymbol{k}_\perp\cdot\boldsymbol{r}_\perp}e_P e^{*}_S e^{*}_I\hat{a}^{\dagger}_{S,k_S}\hat{a}^{\dagger}_{I,k_I}|0\rangle_S|0\rangle_I, \quad (9)$$

where $\Delta k_z = k_P - k_{S_z} - k_{I_z}$ denotes the phase mismatch along z-axis, $\Delta\boldsymbol{k}_\perp$ represents the phase mismatch on the two-dimensional xOy plane, and the loss of pump light α_P has been neglected. Considering the six possible paths of two-photon propagation, we can separate $|\psi\rangle$ into six parts

$$\begin{aligned}|\psi\rangle &\propto \iint_{Br_1}\mathrm{d}k_S\,\mathrm{d}k_I\cdots\hat{a}^{\dagger}_{S,k_S}\hat{a}^{\dagger}_{I,k_I}\\ &\approx \iint_{\Delta k_1=0}\mathrm{d}k_{S,\theta_1}\,\mathrm{d}k_{I,\theta_1+\pi}\cdots\hat{a}^{\dagger}_{S,\theta_1,k_S}\hat{a}^{\dagger}_{I,\theta_1+\pi,k_I}\\ &\quad+\iint_{\Delta k_2=0}\mathrm{d}k_{S,\theta_2}\,\mathrm{d}k_{I,\theta_2+\pi}\cdots\hat{a}^{\dagger}_{S,\theta_2,k_S}\hat{a}^{\dagger}_{I,\theta_2+\pi,k_I}\\ &\quad+\cdots\\ &\quad+\iint_{\Delta k_6=0}\mathrm{d}k_{S,\theta_6}\,\mathrm{d}k_{I,\theta_6+\pi}\cdots\hat{a}^{\dagger}_{S,\theta_6,k_S}\hat{a}^{\dagger}_{I,\theta_6+\pi,k_I}. \quad (10)\end{aligned}$$

Moreover, we go from the k-space to the ω-space, with the relation $\mathrm{d}k = \frac{n_g}{c}\mathrm{d}\omega$ and $\hat{a}_{m,\omega} = \hat{a}_{m,k}\frac{\mathrm{d}k}{\mathrm{d}\omega}$, then we can derive

$$\begin{aligned}|\psi\rangle \propto \iint \mathrm{d}\omega_S\,\mathrm{d}\omega_I\{&A_1(\omega_S,\omega_I)|S,\theta_1,\omega_S\rangle|I,\theta_1+\pi,\omega_I\rangle\\ &+A_2(\omega_S,\omega_I)|S,\theta_2,\omega_S\rangle|I,\theta_2+\pi,\omega_I\rangle\\ &+A_3(\omega_S,\omega_I)|S,\theta_3,\omega_S\rangle|I,\theta_3+\pi,\omega_I\rangle\\ &+A_4(\omega_S,\omega_I)|S,\theta_1+\pi,\omega_S\rangle|I,\theta_1,\omega_I\rangle\\ &+A_5(\omega_S,\omega_I)|S,\theta_2+\pi,\omega_S\rangle|I,\theta_2,\omega_I\rangle\\ &+A_6(\omega_S,\omega_I)|S,\theta_3+\pi,\omega_S\rangle|I,\theta_3,\omega_I\rangle\}, \quad (11)\end{aligned}$$

where

$$A_1(\omega_S,\omega_I) = \sqrt{\omega_S\omega_I}A_P\frac{\mathrm{e}^{\mathrm{i}\Delta k_z L}-1}{\mathrm{i}\Delta k_z}\int\mathrm{d}^2\boldsymbol{r}_{\perp 1}\sum\chi^{(2)}(x,y) \times\mathrm{e}^{\mathrm{i}\Delta\boldsymbol{k}_{\perp 1}\cdot\boldsymbol{r}_{\perp 1}}e_P e^{*}_S e^{*}_I$$

is JSA for the process where the signal photon propagates along path θ_1 and the idler photon propagates along path $\theta_1+\pi$, $|S,\theta_1,\omega_S\rangle=\hat{a}^*_{S,k_S,\theta_1}|0\rangle_S$, and $|I,\theta_1+\pi,\omega_I\rangle=\hat{a}^*_{I,k_I,\theta_1+\pi}|0\rangle_I$. The phase mismatch on the xOy plane for this process is denoted as $\Delta\boldsymbol{k}_{\perp 1}$. $A_2(\omega_S,\omega_I),\ldots,A_6(\omega_S,\omega_I)$ can be obtained similarly.

The photon flux can be estimated by[39–41]

$$\text{Flux}=\langle\psi|\hat{a}^\dagger_S\hat{a}_S|\psi\rangle/S_{\text{eff}}=\frac{8\pi^2 d_{33}^2\omega_S\omega_I LP}{\epsilon_0(n_S n_P n_I)^2 S_{\text{eff}}^2\lambda_P^2\omega_P^2},\quad(12)$$

where P is input pump power, and S_{eff} is the spot area of the pump light. We set $P=1$ mW, $S_{\text{eff}}=0.01$ mm^2 and $L=1$ mm. The second-order nonlinear coefficient $d_{33}=25$ pm/V. $\omega_P=2.4303\times10^{15}$ rad/s, $\omega_S=2\pi f_2=1.2309\times10^{15}$ rad/s and $\omega_I=2\pi f_1=1.1995\times10^{15}$ rad/s are angular frequencies of pump light, signal light and idler light, respectively. Then we find the photon flux of our source scheme to be 2.068×10^5 pairs·s^{-1}·mm^{-2}.

Equation (11) can be written in another form in order to describe the generated biphoton state more explicitly

$$|\psi\rangle\propto\Big(\sum_{i=1}^{3}|\theta_{i,S},(\theta_i+\pi)_I\rangle\Big)\otimes\big(|\omega_{1,S},\omega_{2,I}\rangle+|\omega_{2,S},\omega_{1,I}\rangle\big).\quad(13)$$

Equation (13) is the final expression of our path–frequency hyperentangled biphoton state.

4. Frequency correlations of two-photon pairs

We theoretically calculate the JSA of the generated photon pair, as shown in Fig. 6. Specifically, we set the full width at half maxima (FWHM) of the input continuous pump light to 0.1 nm. The frequency center of the simulated JSA is $f_P/2$, the bandwidth is 8 THz, and the momentum mismatch Δk is fixed at 0.0443 μm^{-1}. We should note that the FWHM of the pump light needs to be narrow enough to ensure high degree of entanglement. In practice, the lattice structure parameters of nonlinear photonic crystals require very precise fabrication, as it directly affects Δk that the crystal can provide, thereby affecting the conversion efficiency of nonlinear processes.

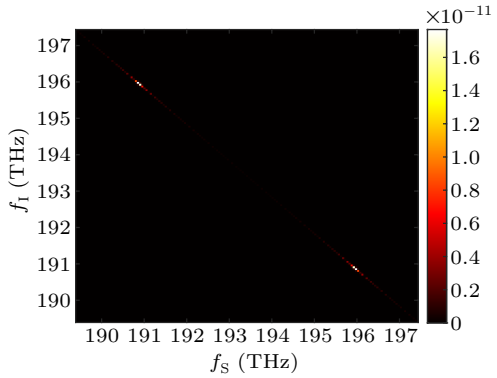

Fig. 6. JSA ($A(\omega_S,\omega_I)$) of the generated hyperentangled photon pair.

To investigate frequency entanglement property, we can perform Schmidt decomposition on $A(\omega_S,\omega_I)$, that is,[42] $A(\omega_S,\omega_I)=\sum_{n=1}^{N}\sqrt{\lambda_n}\psi_n(\omega_S)\phi_n(\omega_I)$, where λ_n is called Schmidt coefficient, and $\psi_n(\omega_S)$ and $\phi_n(\omega_I)$ are a set of standard orthogonal functions. λ_n, $\psi_n(\omega_S)$ and $\phi_n(\omega_I)$ are solutions of the following integral eigenvalue equations:[42]

$$\begin{aligned}\int K_1(\omega,\omega')\psi_n(\omega')\mathrm{d}\omega'&=\lambda_n\psi_n(\omega),\\ \int K_2(\omega,\omega')\phi_n(\omega')\mathrm{d}\omega'&=\lambda_n\phi_n(\omega),\end{aligned}\quad(14)$$

with $K_1(\omega,\omega')\equiv\int A(\omega,\omega_2)A^*(\omega',\omega_2)\mathrm{d}\omega_2$ and $K_2(\omega,\omega')\equiv\int A(\omega_1,\omega)A^*(\omega_1,\omega')\mathrm{d}\omega_1$.

The first 12 Schmidt coefficients, arranged from largest to smallest, are shown in Fig. 7(a). Note that the latter coefficients are close to 0 and their contributions to the degree of entanglement are negligible. Because $A(\omega_S,\omega_I)$ is symmetric with respect to $f_P/2$, Schmidt coefficients always appear in pairs, that is, $\lambda_{2k}=\lambda_{2k+1}(k\in Z)$. Based on the eigenvalue λ_n obtained from the Schmidt decomposition, we can calculate the entropy S of entanglement and effective Schmidt rank K to characterize the degree of frequency entanglement, which are defined as

$$S=-\sum_{n=1}^{N}\lambda_n\log_2\lambda_n,\quad(15)$$

$$K=\frac{(\sum_{n=1}^{N}\lambda_n)^2}{\sum_{n=1}^{N}\lambda_n^2},\quad(16)$$

respectively. $S>0$ and $K>1$ both indicate the presence of entanglement, and the larger value indicates the higher degree of entanglement. The JSA is first normalized and then solved to obtain the Schmidt coefficients in the Schmidt decomposition. The calculated effective Schmidt rank $K=6.4675>1$, and S finally converges to 3.2789, demonstrating strong frequency correlation between the generated two photons around two discrete frequencies f_1 and f_2. Figure 7(b) shows the first 30 iterations of S.

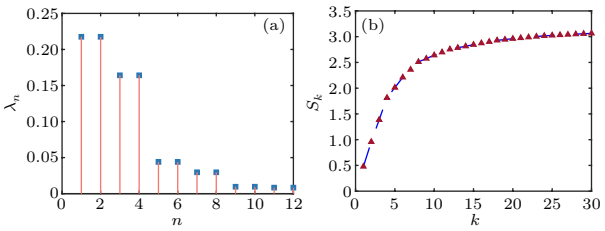

Fig. 7. (a) The maximum 12 Schmidt coefficients. Schmidt coefficients appear in pairs because of the symmetry with respect to $f_P/2$ of $A(\omega_S,\omega_I)$. (b) The first 30 iterations of entropy S of entanglement.

The first eight basis functions in the Schmidt decomposition are shown in Fig. 8, from which we can see the orthogonality of each basis function. Because of the symmetry with respect to $f_P/2$ of $A(\omega_S,\omega_I)$, ψ_n and ϕ_n are divided into two groups, distributed around f_1 and f_2, respectively. It is worth mentioning that ψ_n and ϕ_n have the same shape due to type-I quasi-phase-matching conditions, which means that both signal and idler photons have the same ordinary field mode.

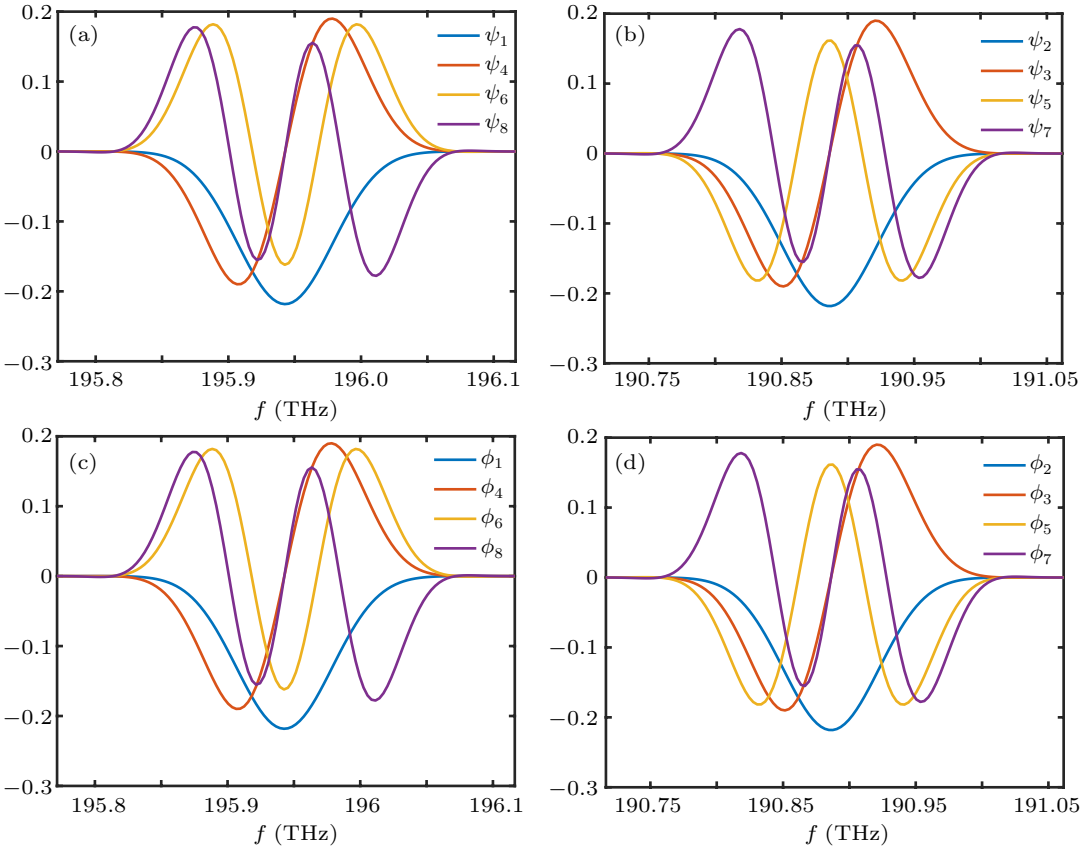

Fig. 8. The first eight basis functions (a) and (b) ψ_n and (c) and (d) ϕ_n.

5. Conclusion

We propose a compact path–frequency hyperentangled quantum light source based on type-I quasi-phase-matched NPC. A two-dimensional periodical $\chi^{(2)}$ NPC is designed to realize quasi-phase-matching in the plane perpendicular to the incident pump beam, including six different paths and two different frequencies. We derive the theoretical expression for the generated two-photon state in detail and estimate the photon flux of our source, which can reach 2.068×10^5 pairs·s^{-1}·mm^{-2}. JSA has been calculated and the resulting entropy S of entanglement and effective Schmidt rank K are 3.2789 and 6.4675, respectively, indicating strong frequency correlation between the generated two photons. As NPC manufacturing technology continues to advance, the possibilities for our two-dimensional NPC scheme are expanding into three dimensions.[34] This advancement opens up promising avenues for future applications in quantum holography, quantum information processing, and long-distance quantum communication.

Acknowledgments

Project supported by the Key-Area Research and Development Program of Guangdong Province of China (Grant No. 2018B030325002), the National Natural Science Foundation of China (Grant No. 62075129), the Open Project Program of SJTU-Pinghu Institute of Intelligent Optoelectronics (Grant No. 2022SPIOE204), the Science and Technology on Metrology and Calibration Laboratory (Grant No. JLJK2022001B002), and the Sichuan Provincial Key Laboratory of Microwave Photonics (Grant No. 2023-04).

References

[1] Madsen L S, Laudenbach F, Askarani M F, Rortais F, Vincent T, Bulmer J F, Miatto F M, Neuhaus L, Helt L G, Collins M J, Lita A E, Gerrits T, Nam S W, Vaidya V D, Menotti M, Dhand I, Vernon Z, Quesada N and Lavoie J 2022 *Nature* **606** 75
[2] Zhong H S, Wang H, Deng Y H, Chen M C, Peng L C, Luo Y H, Qin J, Wu D, Ding X and Hu Y 2020 *Science* **370** 1460
[3] Arrazola J M, Bergholm V, Brádler K, *et al.* 2021 *Nature* **591** 54
[4] Lee N, Benichi H, Takeno Y, Takeda S, Webb J, Huntington E and Furusawa A 2011 *Science* **332** 330
[5] Bennett C H and Wiesner S J 1992 *Phys. Rev. Lett.* **69** 2881
[6] Zhao J J, Guo X M, Wang X Y, Wang N, Li Y M and Peng K C 2013 *Chin. Phys. Lett.* **30** 060302
[7] Zhang Z, Yuan C, Shen S, Yu H, Zhang R, Wang H, Li H, Wang Y, Deng G, Wang Z, You L, Wang Z, Song H, Guo G and Zhou Q 2021 *NPJ Quantum Inf.* **7** 123
[8] Silberhorn C, Korolkova N and Leuchs G 2002 *Phys. Rev. Lett.* **88** 167902
[9] Ekert A K 1991 *Phys. Rev. Lett.* **67** 661
[10] Brida G, Genovese M and Ruo Berchera I 2010 *Nat. Photonics* **4** 227
[11] Defienne H, Ndagano B, Lyons A and Faccio D 2021 *Nat. Phys.* **17** 591
[12] Giovannetti V, Lloyd S and Maccone L 2004 *Science* **306** 1330
[13] Appas F, Baboux F, Amanti M I, Lemaítre A, Boitier F, Diamanti E and Ducci S 2021 *NPJ Quantum Inf.* **7** 118
[14] Hu X M, Zhang C, Guo Y, Wang F X, Xing W B, Huang C X, Liu B H, Huang Y F, Li C F, Guo G C, Gao X, Pivoluska M and Huber M 2021 *Phys. Rev. Lett.* **127** 110505

[15] Levine Y, Sharir O, Cohen N and Shashua A 2019 *Phys. Rev. Lett.* **122** 065301
[16] Zhang Y S, Li C F and Guo G C 2001 *Phys. Rev. A* **64** 024302
[17] Barreiro J T, Langford N K, Peters N A and Kwiat P G 2005 *Phys. Rev. Lett.* **95** 260501
[18] Xie Z, Zhong T, Shrestha S, Xu X, Liang J, Gong Y X, Bienfang J C, Restelli A, Shapiro J H, Wong F N C and Wei W C 2015 *Nat. Photonics* **9** 536
[19] Kim J H, Kim Y, Im D G, Lee C H, Chae J W, Scarcelli G and Kim Y H 2021 *Optica* **8** 1524
[20] Chapman J C, Lim C C W and Kwiat P G 2022 *Phys. Rev. Appl.* **18** 044027
[21] Han Y, Sun Z, Dou T, Wang J, Li Z, Huang Y, Li P and Ma H 2022 *Chin. Phys. Lett.* **39** 070301
[22] Graham T M, Bernstein H J, Wei T C, Junge M and Kwiat P G 2015 *Nat. Commun.* **6** 7185
[23] Vallone G, Ceccarelli R, De Martini F and Mataloni P 2008 *Phys. Rev. A* **78** 062305
[24] Barbieri M, Cinelli C, Mataloni P and De Martini F 2005 *Phys. Rev. A* **72** 052110
[25] Kiess E, Shih Y H, Sergienko A V and Alley C O 1993 *Phys. Rev. Lett.* **71** 3893
[26] Kwiat P G, Mattle K, Weinfurter H, Zeilinger A, Sergienko A V and Shih Y 1995 *Phys. Rev. Lett.* **75** 4337
[27] Eibl M, Gaertner S, Bourennane M, Kurtsiefer C, Żukowski M and Weinfurter H 2003 *Phys. Rev. Lett.* **90** 200403
[28] Barbieri M, De Martini F, Di Nepi G and Mataloni P 2004 *Phys. Rev. Lett.* **92** 177901
[29] Li J, Yuan C, Shen S, Zhang Z, Zhang R, Li H, Wang Y, Deng G, You L, Wang Z, Song H, Fan Y, Guo G and Zhou Q 2023 *Opt. Lett.* **48** 2917
[30] Yang C, Xi C, Jing J and He G 2018 *Opt. Express* **26** 27945
[31] Yu X Q, Xu P, Xie Z D, Wang J F, Leng H Y, Zhao J S, Zhu S N and Ming N B 2008 *Phys. Rev. Lett.* **101** 233601
[32] Chen Y 2015 *Microelectron. Eng.* **135** 57
[33] He J, Tang S H, Qin Y Q, Dong P, Zhang H Z, Kang C H, Sun W X and Shen Z X 2003 *J. Appl. Phys.* **93** 9943
[34] Zhang Y, Sheng Y, Zhu S, Xiao M and Krolikowski W 2021 *Optica* **8** 372
[35] Xu X, Wang T, Chen P, Zhou C, Ma J, Wei D, Wang H, Niu B, Fang X, Wu D, Zhu S, Gu M, Xiao M and Zhang Y 2022 *Nature* **609** 496
[36] Cai W H, Wei B, Wang S and Jin R B 2020 *J. Opt. Soc. Am. B* **37** 3048
[37] Sun Y, Sun C W, Zhou W, Yang R, Duan J C, Gong Y X, Xu P and Zhu S N 2023 *Chin. Phys. B* **32** 080308
[38] Saravi S, Pertsch T and Setzpfandt F 2017 *Phys. Rev. Lett.* **118** 183603
[39] Gong Y X, Xie Z D, Xu P, Yu X Q, Xue P and Zhu S N 2011 *Phys. Rev. A* **84** 053825
[40] Rueda A, Sedlmeir F, Kumari M, Leuchs G and Schwefel H G L 2019 *Nature* **568** 378
[41] Chen N, Wang Z, Wu J, Li H, He S, Fan Z, Fan Y, Zhang X, Zhou Q and Xu J 2023 *Opt. Lett.* **48** 5355
[42] Law C K, Walmsley I A and Eberly J H 2000 *Phys. Rev. Lett.* **84** 5304